Improvement in Determination of Ice Water Content from Two-Dimensional Particle Imagery. Part I: Image-to-Mass Relationships

BRAD BAKER AND R. PAUL LAWSON

SPEC, Inc., Boulder, Colorado

(Manuscript received 29 December 2004, in final form 23 January 2006)

ABSTRACT

Ice water content in natural clouds is an important but difficult quantity to measure. The goal of a number of past studies was to find average relationships between the masses and lengths of ice particles to determine ice water content from in situ data, such as those routinely recorded with two-dimensional imaging probes. The general approach in these past studies was to measure maximum length L and mass M of a dataset of ice crystals collected at a ground site. Linear regression analysis was performed on the logarithms of the data to estimate an average mass-to-length relationship of the form $M = \alpha L^{\beta}$. Relationships were determined for subsets of the dataset based on crystal habit (shape) as well as for the full dataset. In this study, alternative relationships for determining mass using the additional parameters of width W, area A, and perimeter P are explored. A 50% reduction in rms error in the determination of mass relative to using L alone is achieved using a single parameter that is a combination of L, W, A, and P. The new parameter is designed to take into account the shape of the ice particle without the need to classify the crystals first. An interesting result is that, when applied to the test dataset, the same reduction in rms error is also shown to be achievable using A alone. Using A alone facilitates the reanalysis and improvement of the determination of ice water content from large existing datasets of two-dimensional images, because A is simply the number of occulted pixels in the digital images. Possible sources of error in this study are investigated, as is the usefulness of first segregating the particles into crystal habits.

1. Introduction

The ice water content (IWC) of natural clouds is a quantity that is fundamental to several disciplines in the atmospheric sciences, including studies of the formation of the ice phase and precipitation, radiative transfer, cloud chemistry, and numerical models that include cold cloud processes.

Airborne techniques to measure IWC vary but are fundamentally based on two approaches. In one approach, the mass of ice in a known volume of cloudy air is melted and then vaporized. Ice mass is related to measurement of the ice vaporization process, either by measuring the vapor added to the sample volume (e.g., Twohy et al. 1997), or by measuring the latent heats of melting and/or vaporization provided by one or more substrates (Korolev et al. 1998). The second approach involves digital images of ice particles in a known volume of cloudy air. The mass is related to the shape and size of the particle images (e.g., Mason 1957; Brown and Francis 1995; Mitchell et al. 1990, hereinafter M90).

Both approaches have inherent uncertainties. The first approach is generally considered more direct and accurate. For example, Heymsfield et al. (2002, hereinafter H02) used a first-approach technique to validate their second-approach technique. The instrumentation used to digitally record two-dimensional (2D) cloud particle images has been readily available for the past 30 yr, for example, the cloud particle (2D-C) and precipitation particle (2D-P) probes described in Knollenberg (1970, 1981). As a result, there are large existing datasets of 2D images that can be reanalyzed if improved particle image–to-mass algorithms can be identified. Improvement of image-to-mass algorithms, the major contributor to uncertainty in the second approach, is the subject of this work.

Simple power-law relationships relating mass M to length L have been used because M and L are roughly correlated and L is easily measured from imaging probe

Corresponding author address: R. Paul Lawson, SPEC, Inc., 3022 Sterling Circle, Suite 200, Boulder, CO 80301.
E-mail: plawson@specinc.com

data. However, particle area A, width W, and perimeter[1] P, as well as L, are now routinely estimated from imaging probe data. The goal of this work is to explore the improvement possible using this fuller set of parameters instead of just length alone. The applicability of the segregation by the habit approach used by M90 is also explored. The M90 dataset is used in this study. Such data are rare because the mass as well as image is needed. The original M90 dataset has been extended by including images of crystals and their associated melted drops that were collected in 1987, but were not processed until now. A companion paper (Lawson and Baker 2006) will compare the new relationships found here with other relationships previously used in the literature.

2. Technique

The literature contains a number of size-to-mass relationships based on a categorization of the particle type and the maximum dimension of the particle (Mason 1957; Bashkirova and Pershina 1964; Davis 1974; Locatelli and Hobbs 1974; M90; Brown and Francis 1995). All of these relationships take the form

$$M = \alpha L^{\beta}, \tag{1}$$

where M is particle mass, L is particle length, and α and β are constants determined by linear regression. In this study, this approach is extended using the dataset of M90.

The data M90 dataset was originally obtained by collecting ice particles falling from winter storms onto petri dishes positioned near the surface in the Sierra Nevada of California in 1987. The ice particles were photographed under a microscope, melted, and the resulting drops were photographed. Later, the photographic slides were analyzed to categorize the ice particles, and to measure their maximum length and the mean diameter of the melted drops. The mass was calculated assuming a hemispherical drop shape. For each crystal category a least squares linear regression was performed on the logarithms of M and L to create power-law fits as in (1). There were 17 categories used that represent much of the variety of crystal types found in midlatitude winter storms. The crystal types typical of high-altitude cirrus, that is, bullet rosettes and similar spatial crystals, are not represented in this dataset.

In this study, their work is built upon by including not only L, but also W, A, and P in the analysis. The advantages of the new formulation are 1) improved estimates of ice particle masses and 2) a single image-to-mass relationship that translates a two-dimensional particle image to mass, without having to sort the images into particle habits, which is often an intractable process. Also, the M90 dataset is expanded to include crystals that were collected in 1987 but were not analyzed until now.

Figure 1 shows examples from M90 of ice particle images and their drops after melting. A set of fifty-one 35-mm photographic slides of ice particles and associated melted drop data that were collected during the winter of 1986/87 was obtained from Dr. Mitchell of the Desert Research Institute. The 35-mm photographic slides were digitally scanned and the images were processed using an existing SPEC, Inc., software program named CPIview, which is used to process data from cloud particle imager (CPI) probes (Lawson et al. 2001). CPIview derives a number of parameters from the images, including L, W, A, and P; L is the length of the longest cord, and W is the length of the longest cord that is perpendicular to the L cord. These parameters are shown pictorially in Fig. 1.

M90 processed 831 of the images on the fifty-one 35-mm photographic slides. Of these 831, 630 were segregated into 17 habit (shape) categories and used in their study. For this study 549 of the 831 ice particles and equivalent melted drop images that we could unambiguously identify and process with CPIview were selected for reanalysis. An additional 315 images that had not been processed by M90 were processed by SPEC personnel, bringing the total number of images processed in this study to 864. To process additional images it was necessary to be able to properly estimate the masses from the drop images. To be certain that we could accurately reproduce the technique used by M90, we estimated diameters and masses of 21 drops from the images M90 had analyzed and compared the estimates with M90's values. As shown in Fig. 2, our estimates are very close to those of M90, thereby estab-

[1] Perimeter values vary with the technique used. Therefore, a brief description of our perimeter method follows. The first few image processing steps involve the subtraction of the background, using a previously captured reference frame, followed by filtration of the image to reduce the effects of noise (using both median and statistical filters). The resulting image is then thresholded and binarized such that shadows (dark regions relative to the background) become the only remaining features in the image. The outline of these features is then found by computing the custer (Russ 1995, p. 425). A final step discriminates between outline pixels that are inside the feature, versus ones that actually make up the outer perimeter. Then, the perimeter is computed by determining the chain code representation of the perimeter pixels and counting orthogonal and diagonal occurrences (Russ 1995, 509–510).

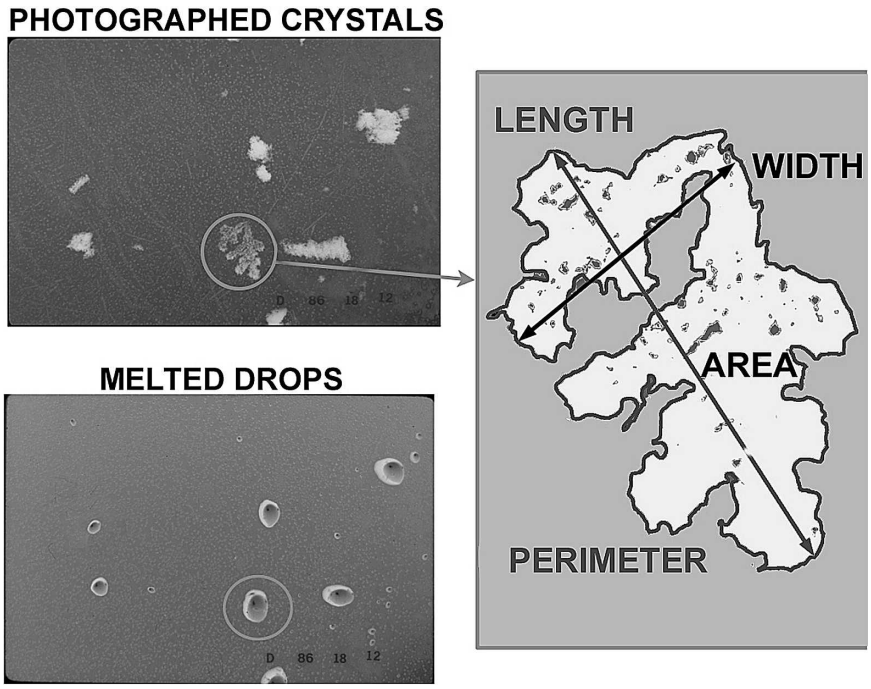

FIG. 1. Examples, from M90, of images of crystals and their drops after melting. Also shown is an example of the CPIview-derived parameters L, W, A, and P.

lishing confidence that we could extend the M90 dataset while maintaining experimental continuity.

Two measures were chosen with which to quantify the improvement achieved using the additional parameters. These relate to two basic types of error. One type of error is simply the difference between the masses estimated from the drop diameters, which for simplicity are referred to as the actual masses, and the masses estimated using the image-to-mass relationship (1). This will be referred to as type-I error and will be represented with the rms differences and the correlation coefficient.[2] The other error is in the robustness of the image-to-mass relationships; or, in other words, how accurately β was found from the limited dataset. This will be referred to as type-II error. It is explored using a bootstrap analysis (Efron and Tibshirani 1993). Bootstrap methods use randomly selected subsets of the dataset to recalculate a parameter of interest many times, in this case β. The uncertainty in β is calculated as the standard deviation divided by the mean of the bootstrapped βs. This is multiplied by 100 to convert it to a percentage.

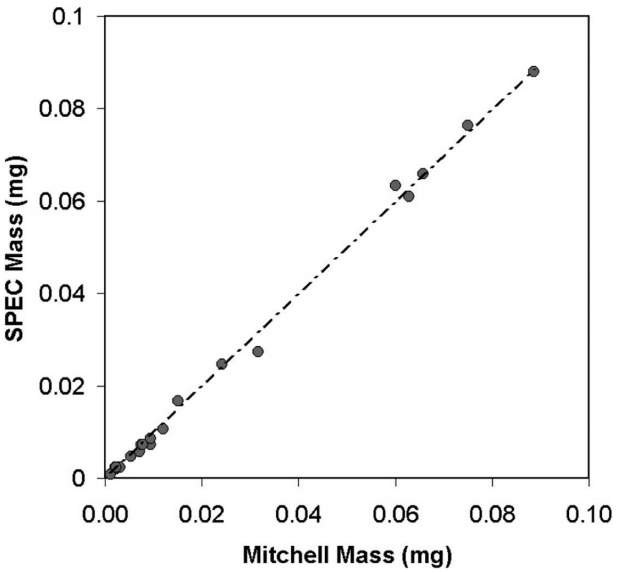

FIG. 2. Masses of 21 drops estimated from their diameters by SPEC vs the same estimated by M90.

[2] The correlation coefficient R and rms error of a least squares linear regression are directly related. The square of the correlation coefficient is the fraction of the predicted variable's variance that is explained by the linear relationship. The rms error squared is the remainder of that variance; rms error $= [(1 - R^2)\mathrm{Var}(M)]^{1/2}$. The figures display R^2 of the least squares linear regression of the "logarithms" of M and whatever variable is being used to predict M. The displayed rms error, however, is calculated from the actual and predicted values of M, not their logarithms. Thus, though still related, the values of R^2 and rms error shown in the figures are not related by the above equation.

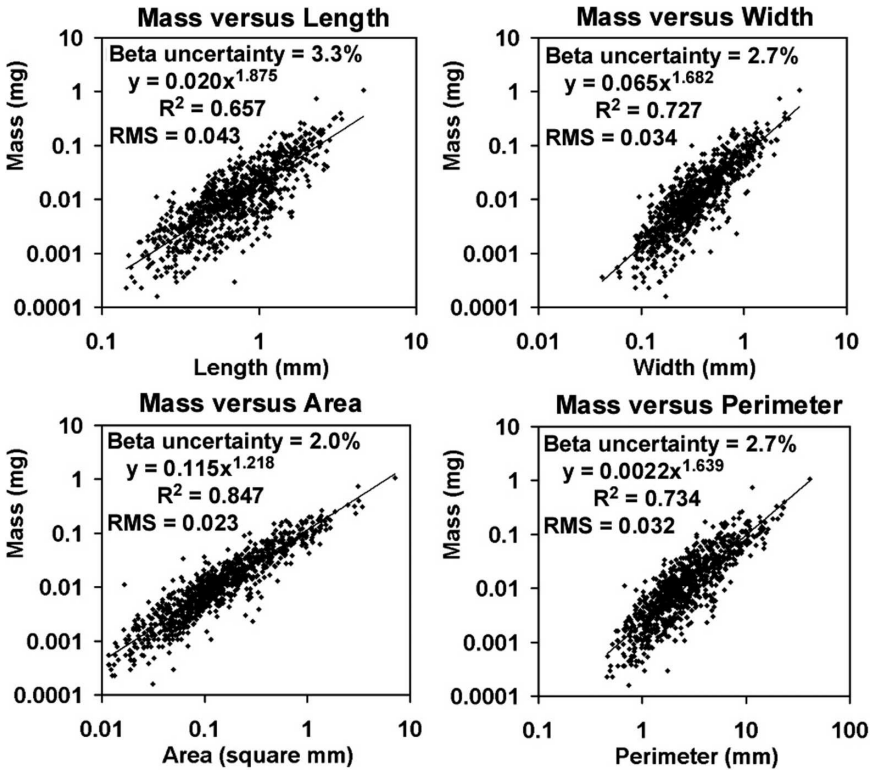

FIG. 3. Log–log plots of mass vs each of the various individual size parameters L, W, A, and P. The least squares regression line, equation, and correlation coefficient squared are shown along with the rms error. The latter is calculated from the values themselves, not from their logarithms.

Type-I error influences how many particles must be averaged together to obtain an acceptable estimate of IWC, assuming the relationship is correct, on average. Type-II error is associated with whether the image-to-mass relationship is correct on average when extended to other similar data.

3. Results

a. Individual parameter fits

First, each of the individual size parameters are compared using the same power-law least squares linear regression method that M90 used for L. The results are shown in Fig. 3. It is seen that W and P predict the mass about equally well and about 25% better than L. Area A is by far the best single predictor, with nearly a 50% reduction in rms error relative to use of L.

b. A combined parameter fit

Using the four individual size parameters L, W, A, and P, we created a combined single parameter (CSP) as

$$\mathrm{CSP} = AW(2L + 2W)/P. \quad (2)$$

The following reasoning was used to formulate this parameter: A estimates the solid part of the particle on the 2D image, W estimates its extension out of the 2D plane, and $(2L + 2W)/P$ reflects its decreased average density when its perimeter is convoluted. Other formulations are certainly possible. We experimented with others but without improvement.

Because CSP is still a single parameter, it can be applied and evaluated in the same manner as the individual parameters shown in Fig. 3. That is, α and β were determined by least squares linear regression on the logarithms of M and CSP. The results of applying and evaluating the combined single parameter are shown in Fig. 4.

The combined single parameter does not represent significant improvement relative to using area alone. However, because it depends on more parameters, it may be more likely, than A alone, to retain accuracy when applied to new datasets that contain a wider diversity of particle shapes. This hypothesis is discussed further in section 4 where errors are discussed, but ultimately it remains to be investigated when more data are available.

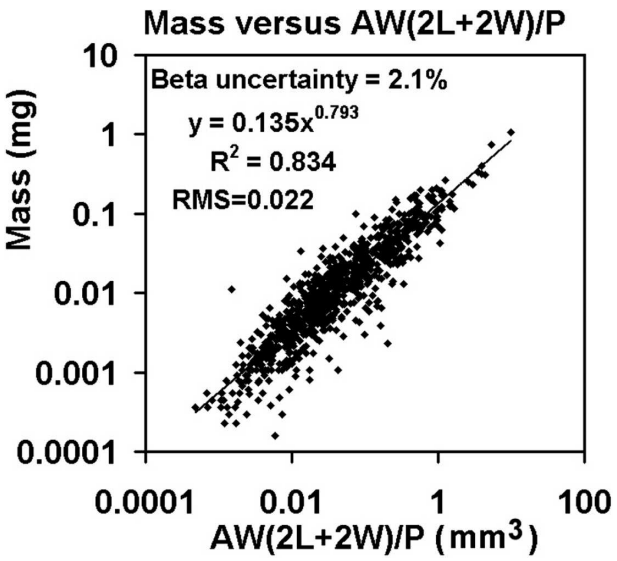

FIG. 4. As in Fig. 3, but for the combined single parameter $AW(2L + 2W)/P$.

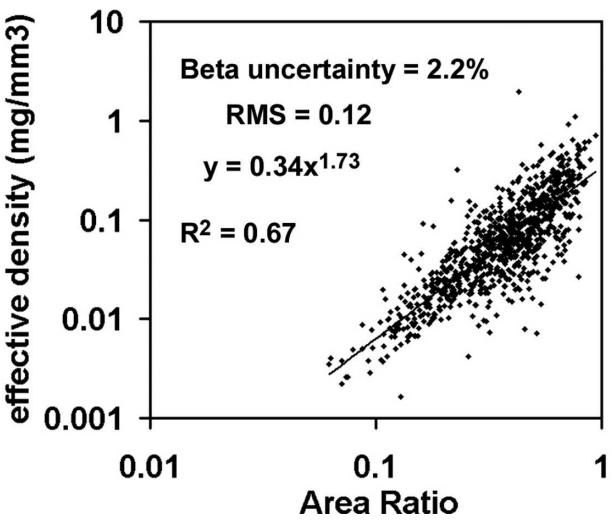

FIG. 5. As in Fig. 3, but the effective density is fit to the area ratio. The rms error is still calculated from the estimated masses vs the true masses.

c. Another combined parameter fit

H02 also included area together with length and improved IWC estimates from 2D image data for certain crystal types. In their approach a power-law relationship ($\rho_e = \alpha A_r^\beta$) between area ratio A_r and effective density ρ_e was determined for various crystal types, where

$$A_r \equiv \frac{A}{(\pi/4)L^2} \quad \text{and} \quad \rho_e \equiv \frac{M}{(\pi/6)L^3}. \tag{3}$$

The mass of a crystal is then estimated from ρ_e and its size, if its type is known and is one for which a relationship was established. To be specific, because $\rho_e = \alpha A_r^\beta$ by substitution we obtain

$$M = 6^{-1} \times 4^\beta \pi^{1-\beta} \alpha A^\beta L^{3-2\beta}. \tag{4}$$

H02 established relationships (i.e., values of α and β) for columnar, planar, spatial rosette, side plane, and aggregate-type ice crystals via a complex combination of theoretical derivations based on simple ideal shapes, the numerical modeling of more complex shapes, and the incorporation of fits from various sets of observational data.

H02 applied the method to calculate IWCs in clouds from in situ image data and compared the results with a more direct measure of the ice water content. Because the method requires habit classification and relationships for each habit class, they were only able to do this to limited datasets. Specifically, two examples of cirrus cloud data dominated by bullet rosettes and one example dominated by a side plane were presented. The results in those special cases were very promising, and the approach of predicting ρ_e from A_r instead of M directly from the size parameters is very appealing. To investigate the possibility that the H02 technique would perform as successfully when applied to a general dataset, the H02 approach was applied to the expanded M90 dataset without habit classification. Figure 5 shows the result.

A least squares linear regression was performed on the logarithms of ρ_e and A_r. The data, the best-fit equation, the square of the correlation coefficient, and the uncertainty in β are all shown on the figure. Masses were then estimated. The rms error for the masses is also shown on the figure. For this data, it does not appear that this approach is better than predicting M directly from the size parameters. The β uncertainty is similar to those for CSP and the A to M fits presented above. However, the correlation coefficient is lower, which suggests that ρ_e is not as predictable from A_r as M is from A or CSP. In addition, the rms error is much larger for the H02 method applied to the expanded M90 dataset.

For the same dataset, the rms error for the H02 method is expected to be greater than for the CSP and A methods. This is because for the CSP and A methods, the mass rms error is minimized by the least squares regression, whereas for the H02 method applied here, it is the effective density rms differences that are minimized by the least squares regression. Thus, it could be argued that the H02 method would extend more successfully to a different but similar dataset. To address this possibility, a special comparison was made whereby

TABLE 1. A comparison of M90's habit-conditioned results with results of three non-habit-conditioned techniques. Each technique's equation(s), although derived from larger datasets, was applied only to the 444 particles that were originally processed by M90, classified as one of the 17 categories used in M90, and reprocessed by SPEC. This procedure was followed because in order to make this comparison the particles must have been classified as a certain type (done only in M90) and also have the additional parameters W, A, and P (via SPEC reprocessing).

Method	Equation	Rms error (mg)	β uncertainty
Least squares (LS) fit w.r.t. L (M90)	$0.021L^{2.0}$	0.0396	2.7%
17 habit-conditioned LS fits w.r.t. L (M90)	See Table 2	0.0280	See Table 2
Least squares fit w.r.t. A	$0.115A^{1.218}$	0.0262	2.0%
Least squares fit w.r.t. CSP	$0.135X^{0.793}$	0.0255	2.1%

the dataset was repeatedly split into random halves. For each split the regression fits were applied as before to one-half of the data. The derived equations were then applied to the other one-half of the data, and the rms error for the predicted masses were calculated only for this half. The average rms errors calculated this way for the CSP case, the A case, and the H02 method applied to the expanded M90 dataset were not significantly different than those reported in Figs. 3, 4, and 5 that were calculated using the entire dataset. Therefore, the possibility that the H02 technique would perform better on a different, but similar, dataset was addressed, and it still does not appear to be advantageous to predict ρ_e from A_r, instead of M directly, from the various size parameters.

d. Multiple parameter fits

Approaches more sophisticated than the linear regression of single parameters can be applied (e.g., multivariate regressions and neural networks), but so far we have found only very limited improvement, if any, using these approaches. It remains to be determined whether this is a limitation attributable to the nature of predicting mass from 2D image information, or whether experimental errors inherent in the techniques of M90 and this study are also responsible. However, in section 4, evidence is presented suggesting that experimental errors in this study may be significant.

e. Multiple parameter fits using habit categorization

Whereas CSP is still mathematically a single parameter and could thus be applied and compared in the same way as the individual parameters (L, W, A, and P), M90 used a different linear regression with respect to L for each of 17 habit classes. Thus, while still using the same technique, it is a multiparameter approach and requires additional work to evaluate. This multiparameter approach was applied and is compared with the single-parameter approaches in Table 1. We emphasize two points, as follows below.

One point is that segregating the data and applying separate fits to each subset will necessarily lower the rms error. This would be true even for random subsets. However, the reduction of rms error achieved by applying 17 fits instead of 1 fit, while significant, is still smaller than the reduction of rms error achieved by using a single fit on A or CSP.

The second point addresses uncertainty in the exponent, that is, the uncertainty in β, used in (1). M90 segregated the data according to shape (habit classification) with the anticipation that each fit would be representative of its class. However, bootstrap analysis of the exponents (βs), shown in Table 2, indicates that the uncertainties are too great to warrant their use, even if routine habit classification were possible. This is because for most of the habit classes, the uncertainty in its individual β is as great or greater than the difference between its β and the β derived from the full (all category) dataset.

It is worth emphasizing here that particle shape is important. The results here show that 1) the CSP and even A alone account for particle shape better than the habit segregation with L alone as the predictor, and 2) the dataset is not extensive enough to derive meaningful separate relationships for each habit class represented. The later point is one reason why the habit segregation approach was not applied using CSP or A as predictors. The other reason is that automatic classification of crystals into habit types is a difficult, if not intractable, problem at present. Therefore, at present, we do not recommend the habit segregation approach.

4. Consideration of errors

Many possible sources of error could be speculated upon in this study. The focus here is on two interrelated but separable issues. The two issues concern mass estimates from drop images and automatic estimation of the crystal image parameters L, W, A, and P.

a. Measurement errors of mass

The experimental errors associated with the dataset of M90, which are extended and used in this study, are

TABLE 2. An analysis of M90's original dataset (630 particles) that was segregated into 17 habit-conditioned subsets. The first column is the habit class; the second is the number of crystals in the subset; the third shows the exponential relationship derived by linear regression; the fourth is the difference between that habit class β and the β derived from all the particles; the fifth is the absolute and percentage uncertainty in β derived from bootstrap analysis.

Crystal type	N	Equation	Difference in β	β uncertainty (%)
All	630	$0.021L^{2.0}$	0.0	0.053 (2.7%)
Elementary needles	16	$0.0048L^{1.8}$	0.2	0.57 (31%)
Rimed elementary needles	7	$0.0059L^{2.1}$	0.1	0.65 (32%)
Long columns	64	$0.012L^{1.9}$	0.1	0.37 (20%)
Rimed long columns	27	$0.023L^{1.8}$	0.2	0.33 (18%)
Combinations of long columns	62	$0.017L^{1.8}$	0.2	0.20 (11%)
Rimed combinations of long columns	54	$0.025L^{1.9}$	0.1	0.14 (7.3%)
Short columns	12	$0.064L^{2.6}$	0.6	0.61 (23%)
Combinations of short columns	17	$0.031L^{1.9}$	0.1	1.6 (88%)
Hexagonal plates	30	$0.028L^{2.5}$	0.5	0.45 (18%)
Radiating assemblages of plates	63	$0.019L^{2.1}$	0.1	0.16 (7.6%)
Side plane	77	$0.021L^{2.3}$	0.3	0.13 (5.5%)
Heavily rimed dendritic crystals	20	$0.068L^{2.2}$	0.2	0.41 (18%)
Fragments of heavily rimed dendritic crystals	39	$0.027L^{1.7}$	0.3	0.38 (22%)
Aggregates of side planes	35	$0.021L^{2.2}$	0.2	0.24 (11%)
Aggregates of side planes, bullets, and columns	31	$0.022L^{2.1}$	0.1	0.23 (11%)
Aggregates of radiating assemblages of plates	30	$0.023L^{1.8}$	0.2	0.22 (12%)
Aggregates of fragments of heavily rimed dendritic crystals	46	$0.034L^{2.0}$	0.0	0.20 (10%)

also important to address. It is possible that the lack of improvement in using A, L, W, and P, relative to using A alone, and the lack of improvement using multivariate techniques, could be because of errors in measuring particle geometries and equivalent masses in the M90 dataset. For example, in M90 the masses are estimated from drop images by assuming the drops are hemispheres. An average diameter was used for drop images that are not circular (viewed from above). The fact that some of the drops were not circular (Fig. 1) suggests that the contact angles could have also varied, causing errors in the mass estimates. There is no way to directly assess the magnitude of this error because individual drop contact angles were not measured.

However assuming a column, viewed from above, is lying flat on one side and is solid, the mass can be found from its length L' and width W' using basic geometry, where the prime denotes the usual definitions of length and width for a rectangle. The masses are compared this way for 17 of the 76 images that M90 classified as single columns and that appeared to us to be approximate simple, solid hexagonal columns. The results are shown in Fig. 6. There is reasonably good correlation in Fig. 6 between the melted drop masses and the masses assuming an ideal solid column shape, with about 30% average error. The error in Fig. 6 is not necessarily all due to error in the mass estimates. Another source of error is the estimates of L' and W'. For Fig. 6, L' and W' were found manually, which is more accurate than automatic methods but is still subjective.

b. Measurement errors of image parameters

Except where specifically mentioned, L, W, A, and P were found automatically using CPIview software. Figures 7a–c show three typical CPI images of crystals collected in clouds, with their perimeters determined automatically using the CPIview software. The values of the ratio $2(L + W)/P$ are also shown. The motivation for including this ratio in CSP is apparent, because the smaller this ratio the lower the effective density of the ice particle. Figure 7d shows a typical image from the M90 dataset and its perimeter, which was also determined automatically using CPIview. Because of the dif-

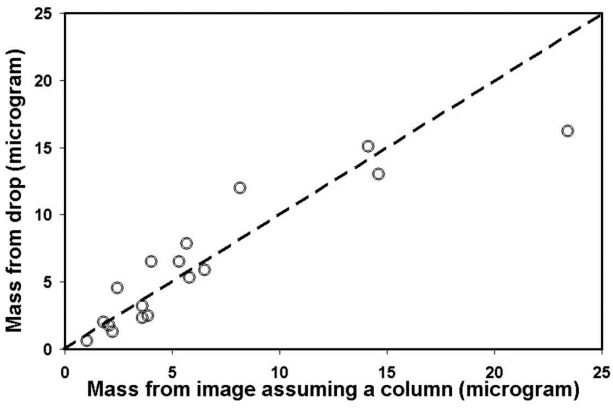

FIG. 6. Scatterplot of the masses derived from the drop images by M90 vs the masses derived from the ice image assuming a solid hexagonal column.

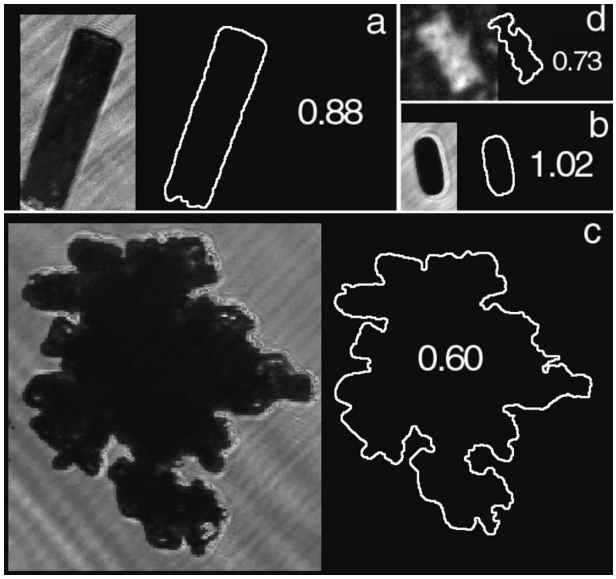

FIG. 7. Various images of natural ice crystals, their perimeters drawn by CPIview, and the value of $2(L + W)/P$: (a), (b), (c) CPI and (d) M90.

ferent medium of the M90 data, the perimeters drawn by CPIview appear to be more convoluted than if they were drawn manually. Thus, there are errors inherent in particle geometry estimates in the automated reanalysis of the M90 dataset. While we are unable to quantify these errors, they may be significant and could be responsible for the limited improvement achievable from this dataset when additional parameters are included (sections 3b and 3d).

Also, the orientation of certain crystal types, such as plates and columns, is not completely random in a petri dish. Their orientation in an imaging probe may be random or biased in a different way than in a petri dish. This fact may imply additional errors in IWC estimates from imaging probe data using the equations derived herein, from petri dish images.

5. Conclusions

This study shows that, as expected, using parameters in addition to L alone yields improved estimates of particle masses. Using A alone to determine mass yields the best estimate of all of the individual size parameters (L, W, A, P) assessed in this study, achieving nearly 50% improvement in rms error over using L alone. The results are not only significantly better than using L alone, but are also significantly better than using 17 distinct mass-to-length relationships based on prior habit classification. It is also shown that most of the habit-conditioned relationships of M90 are not robust. Determination of A from the large existing 2D-C and 2D-P datasets is computationally straightforward (because this is simply the number of occulted pixels), thereby facilitating reanalysis of these data to improve IWC determination.

A single parameter combining A, L, W, and P in a logical combination yielded similar results to using A alone. It is suggested that the lack of better predictions using L, W, A, and P versus A alone could be due to measurement errors in drop masses and ice particle geometries for this limited dataset. Collection of a larger dataset of crystal images and melted drops with reduced measurement errors is needed. This could resolve experimental issues raised in this paper and could provide considerable additional improvement in the determination of IWC from 2D image data, either by the techniques presented herein or by facilitating more sophisticated multivariate approaches. The improved dataset should also include particle types representative of all types of atmospheric ice, in particular cirrus cloud particles, which are not well represented in the current dataset.

Acknowledgments. We thank Dave Mitchell for the use of his data and for his input and support throughout the study. This work was performed under funding from National Science Foundation ATM-9904710, NSF ATM-0244731, NSF OPP-0084314, NASA TRMM NAS5-00244, and NASA NNG04GE71G.

REFERENCES

Bashkirova, G. M., and T. A. Pershina, 1964: On the mass of snow crystals and their fall velocity. *Tr. Gl. Geofiz. Obs. Engl. Transl.,* **165,** 83–100.

Brown, P. R. A., and P. N. Francis, 1995: Improved measurements of the ice water content in cirrus using a total-water probe. *J. Atmos. Oceanic Technol.,* **12,** 410–414.

Davis, C. I., 1974: The ice-nucleating characteristics of various AgI aerosols. Ph.D. dissertation, University of Wyoming, 267 pp.

Efron, B., and R. J. Tibshirani, 1993: *An Introduction to the Bootstrap*. CRC Press, 436 pp.

Heymsfield, A. J., S. Lewis, A. Bansemer, J. Iaquinta, L. M. Miloshevich, M. Kajikawa, C. Twohy, and M. R. Poellot, 2002: A general approach for deriving the properties of cirrus and stratiform ice cloud particles. *J. Atmos. Sci.,* **59,** 3–29.

Knollenberg, R. G., 1970: The optical array: An alternative to scattering or extinction for airborne particle size determination. *J. Appl. Meteor.,* **9,** 86–103.

——, 1981: Techniques for probing cloud microstructure. *Clouds: Their Formation, Optical Properties, and Effects,* P. V. Hobbs and A. Deepak, Eds., Academic Press, 15–91.

Korolev, A. V., J. W. Strapp, G. A. Isaac, and A. N. Nevzorov, 1998: The Nevzorov airborne hot-wire LWC-TWC probe: Principle of operation and performance characteristics. *J. Atmos. Oceanic Technol.,* **15,** 1495–1510.

Lawson, R. P., and B. A. Baker, 2006: Improvement in determination of ice water content from two-dimensional particle imagery. Part II: Applications to collected data. *J. Appl. Meteor. Climatol.,* **45,** 1291–1303.

——, ——, C. G. Schmitt, and T. L. Jensen, 2001: An overview of

microphysical properties of Arctic clouds observed in May and July during FIRE.ACE. *J. Geophys. Res.,* **106,** 14 989–15 014.

Locatelli, J. D., and P. V. Hobbs, 1974: Fall speeds and masses of solid precipitation particles. *J. Geophys. Res.,* **79,** 2185–2197.

Mason, B. J., 1957: *The Physics of Clouds*. Oxford University Press, 671 pp.

Mitchell, D. L., R. Zhang, and R. L. Pitter, 1990: Mass-dimensional relationships for ice particles and the influence of riming on snowfall rates. *J. Appl. Meteor.,* **29,** 153–163.

Russ, J. C., 1995: *The Image Processing Handbook*. 4th ed. CRC Press, 744 pp.

Twohy, C. H., A. J. Schanot, and W. A. Cooper, 1997: Measurement of condensed water content in liquid and ice clouds using an airborne counterflow virtual impactor. *J. Atmos. Oceanic Technol.,* **14,** 197–202.

CORRIGENDUM

BRAD BAKER AND R. PAUL LAWSON

SPEC, Inc., Boulder, Colorado

(Manuscript received and in final form 15 June 2016)

ABSTRACT

Corrections are made to the results, and interpretation thereof, presented in earlier work by Baker and Lawson. The main results regarding the improvement obtained using additional image parameters are unchanged. Secondary results regarding the applicability of subgroup parameterizations are corrected. Whereas it was found in the earlier work that very few subgroup parameterizations could be applied, it is now found that more subgroup parameterizations could be applied in situations in which crystal habits are sufficiently identifiable.

1. Introduction

The ice particle image and mass data of Mitchell et al. (1990, hereinafter M90) and Baker and Lawson (2006, hereinafter BL06) were revisited in a paper by B. Baker and R. P. Lawson (2016, unpublished manuscript, hereinafter BL16) to extend results to large dendritic crystals, which were underrepresented in those previous studies. During this work, errors were discovered in BL06. These errors and their correction are the topic of this corrigendum. The main results of BL06, which are inclusion of mass parameterizations based on the additional image parameters, area, width, and perimeter, are not affected here.

BL06 also presented a bootstrap reanalysis of the dataset used by M90, which parameterized masses M on the basis of image lengths L alone. Those results were presented in Table 2 of BL06. Our corrections here are of the values and interpretation of those results. We concluded that, for the majority of the subgroups, the results were not sufficiently robust and different from the ''all'' category result to support the use of the subgroup results.

This was erroneous for two reasons. First, BL06 did not present the differences and uncertainties of both of the parameters (α and β) in the parameterization $M = \alpha L^{\beta}$. Only the differences and uncertainties of the values for β were presented. As the results of BL16 exemplify, a significant difference in α is all that is required to warrant the use of a subgroup parameterization. Second, the β uncertainties reported in BL06 are not reproducible and are corrected herein. The new values are about two-thirds of the magnitude of those reported in BL06.

2. Corrections

Both errors are corrected in the results shown in Table 1. Table 1 is similar to Table 2 of BL06. The differences are corrected uncertainties in β, which are column 5 in Table 1, and the inclusion of the uncertainties in α, which are column 8. The β uncertainties are estimated through the standard deviation of the β values of 50 000 bootstrapped linear regressions, and the means of the β values for those 50 000 regressions determine the β values themselves. Here, β is the slope m in each linear-regression result $Y = mX + b$, where Y is the natural logarithm of the masses and X is the natural logarithm of the lengths L. Parameter α is

Corresponding author address: Brad Baker, 6905 40th Ave., University Park, MD 20782.
E-mail: brad.aa.baker@gmail.com

DOI: 10.1175/JAMC-D-16-0212.1

TABLE 1. Bootstrap reanalysis of the data of M90. The first column indicates subgroup crystal type, the second column indicates the number of data in the group, the third column presents the power law parameterization of $M(L)$ in the form $M = \alpha L^{\beta}$ determined by least squares linear regression of the logarithms of M and L as described in the text. The fourth column ($\Delta\beta$) is the absolute value of the difference in β between the all-types-above case and each other subgroup. The fifth column is the β uncertainty, and the sixth column is the β ratio, as described in the text. Columns 7–9 are, respectively, the analogous differences, uncertainties, and ratio for α.

Crystal type	N	Equation	$\Delta\beta$	β uncertainty	β ratio	α factors	α uncertainty	α ratio
Elementary needles	16	$0.004\,93L^{1.80}$	0.20	0.33	0.55	4.31	1.12	**3.75**
Rimed elementary needles	7	$0.006\,19L^{2.10}$	0.10	0.27	0.32	3.52	1.16	**2.96**
Long columns	64	$0.0124L^{1.85}$	0.15	0.25	0.54	1.69	1.17	**1.41**
Rimed long columns	27	$0.0233L^{1.83}$	0.17	0.21	0.68	1.11	1.15	*0.94*
Combinations of long columns	62	$0.0167L^{1.83}$	0.18	0.13	*1.03*	1.26	1.08	*1.13*
Rimed combinations of long columns	54	$0.0251L^{1.93}$	0.07	0.09	0.55	1.20	1.08	*1.08*
Short columns	12	$0.0642L^{2.61}$	0.61	0.28	**1.92**	3.05	1.48	**2.00**
Combinations of short columns	17	$0.0298L^{1.88}$	0.12	0.28	0.37	1.42	1.24	*1.11*
Hexagonal plates	30	$0.0274L^{2.47}$	0.47	0.30	**1.39**	1.30	1.29	*0.98*
Radiating assemblages of plates	63	$0.0187L^{2.09}$	0.09	0.11	0.61	1.12	1.06	*1.03*
Side planes	77	$0.0206L^{2.30}$	0.30	0.09	**2.44**	1.02	1.05	*0.94*
Heavily rimed dendritic crystals	20	$0.0717L^{2.23}$	0.23	0.25	*0.79*	3.41	1.23	**2.71**
Fragments of heavily rimed dendritic crystals	39	$0.0268L^{1.71}$	0.29	0.25	*1.00*	1.27	1.23	*1.01*
Aggregates of side planes	35	$0.0212L^{2.17}$	0.17	0.17	*0.82*	1.01	1.15	*0.86*
Aggregates of side planes, bullets, and columns	31	$0.0222L^{2.13}$	0.13	0.15	0.70	1.05	1.12	*0.92*
Aggregates of radiating assemblages of plates	30	$0.0229L^{1.81}$	0.19	0.14	*1.11*	1.09	1.13	*0.94*
Aggregates of fragments of heavily rimed dendritic crystals	46	$0.0341L^{1.96}$	0.05	0.14	0.26	1.63	1.08	**1.46**
All types above	630	$0.0210L^{2.00}$	—	0.04	—	—	1.03	—

similarly estimated as $\alpha = e^{\langle b \rangle}$, where $\langle b \rangle$ represents the average y intercept b of the 50 000 bootstrapped regressions and the α uncertainty is estimated as $e^{[\mathrm{stdev}(b)]}$, where stdev(b) is the standard deviation of the 50 000 bootstrapped linear-regression y intercepts b.

In addition, columns are added to facilitate visualizing for which subgroups the coefficients α and β are significantly different from the "all types above" case. These are columns 6 and 9 for α and β, respectively. For column 6 (labeled β ratio), we divide the differences in the β values between the all-above-types case and the subgroup cases, which is column 4 and is labeled $\Delta\beta$, by the combined β uncertainty estimate for each case, which is column 5 plus 0.0365; 0.0365 is the β uncertainty estimate for the all-types-above case. If the β ratio is significantly greater than 1, then the difference in β values is large relative to their combined uncertainties and we have confidence that the differences in β are real. These cases are in boldface font. If, however, the β ratio is significantly less than 1, then the difference in β values is small relative to their combined uncertainties and we cannot have confidence that the differences in β are real. These cases are in lightface font. For values of β ratio near 1, one has a borderline situation, which is indicated in italic font.

Column 9 (labeled α ratio) is similar to column 6 but for α. Here, in place of $\Delta\beta$, the numerator of the α ratio is taken as the value of α for each subgroup divided by the value of α for the all-types-above case, or its inverse, whichever is larger, that is, greater than 1. This is column 7 and is labeled "α factors." It is calculated as this ratio because α is calculated as $\alpha = e^{\langle b \rangle}$ and because the laws of exponentials and logarithms indicate that subtracting y intercepts ($\langle b \rangle$ values) is equivalent to dividing their α values. In a similar way, the denominator is taken as the product of α uncertainties in place of the sum of β uncertainties. That is, the denominator of the α ratio is taken as the product of subgroup α uncertainties (column 8) and 1.0273, which is the α uncertainty estimate for the all-types-above case.

Just as for the β ratio, if the α ratio is significantly greater than 1, then the difference in α values is large relative to their combined uncertainties and we have confidence that the differences in α are real. These cases are shown in boldface font. If, however, the α ratio is significantly less than 1, then the difference in α values is small relative to their combined uncertainties and we cannot have confidence that the differences in α are real. For values of α ratio values near 1, one again has a borderline situation, which is shown in italic font.

TABLE 2. As in Table 1, but mass M is parameterized as a function of area A instead of length L.

Crystal type	N	Equation	$\Delta\beta$	β uncertainty	β ratio	α factors	α uncertainty	α ratio
Elementary needles	11	$0.0869A^{1.28}$	0.09	0.20	0.41	1.29	1.54	0.80
Rimed elementary needles	6	$0.128A^{1.46}$	0.27	0.85	0.31	1.15	5.39	0.20
Long columns	47	$0.164A^{1.31}$	0.13	0.19	0.59	1.47	1.71	*0.82*
Rimed long columns	26	$0.177A^{1.25}$	0.07	0.10	0.54	1.58	1.19	**1.26**
Combinations of long columns	46	$0.125A^{1.15}$	0.04	0.11	0.28	1.12	1.27	*0.83*
Rimed combinations of long columns	39	$0.117A^{1.09}$	0.09	0.08	*0.86*	1.04	1.18	*0.84*
Short columns	10	$0.418A^{1.63}$	0.44	0.28	**1.45**	3.74	2.23	**1.59**
Combinations of short columns	14	$0.217A^{1.44}$	0.26	0.24	*0.98*	1.94	1.73	*1.06*
Hexagonal plates	17	$0.0502A^{1.18}$	0.01	0.32	0.02	2.22	2.35	*0.90*
Radiating assemblages of plates	36	$0.0567A^{1.03}$	0.15	0.08	**1.41**	1.97	1.17	**1.60**
Side planes	59	$0.109A^{1.24}$	0.06	0.15	0.34	1.02	1.23	0.79
Heavily rimed dendritic crystals	15	$0.186A^{1.22}$	0.04	0.12	0.27	1.66	1.30	*1.21*
Fragments of heavily rimed dendritic crystals	36	$0.0992A^{1.11}$	0.08	0.14	0.46	1.13	1.43	0.75
Aggregates of side planes	17	$0.109A^{1.08}$	0.10	0.07	*1.06*	1.02	1.08	*0.90*
Aggregates of side planes, bullets, and columns	18	$0.112A^{1.07}$	0.11	0.13	0.72	1.00	1.08	*0.88*
Aggregates of radiating assemblages of plates	13	$0.0931A^{1.28}$	0.10	0.13	0.60	1.20	1.12	*1.02*
Aggregates of fragments of heavily rimed dendritic crystals	34	$0.125A^{1.06}$	0.12	0.10	*0.95*	1.12	1.09	*0.98*
All types above	444	$0.112A^{1.18}$	—	0.03	—	—	1.05	—

3. Discussion

From Table 1, we see that, similar to BL06's result, few subgroups (in fact, only three) are well distinguished by their values of β: the short-column, hexagonal-plate, and side-plane subgroups. Six subgroups are distinguished by their values of α: the elementary needles, rimed elementary needles, long columns, short columns, heavily rimed dendritic crystals, and aggregates of fragments of heavily rimed dendritic crystals.

Although the difficulties of automatic habit classification indicate that these subgroup results may not be widely applicable, BL16 demonstrate that in some situations the use of a subgroup result can be warranted and beneficial. Because of that, together with the main result of BL06 that area is a better predictor of mass than length is, we present Table 2. Table 2 is like Table 1 except the predictor is area instead of length.

Note that there are overall fewer data points in Table 2 than in Table 1. This is because only a subset of M90's original data was of sufficient quality that the automatic image processing of BL06, which determined area and perimeter, for example, was deemed acceptable. BL06 then included addition images for their analysis, bringing their total to 864, but those data were not classified by habit and thus could not be included in Table 2. Thus, Table 2 is included because area is a better mass predictor than length, but the caveat that the dataset is reduced must be acknowledged.

In fact, all of the results of M90, BL06, and this corrigendum are subject to the same caveat that the results are not expected to be applicable, with high accuracy, to general ice-crystal datasets. However, until such time as more broadly representative datasets are obtained and analyzed, these types of results, with/despite their caveats, are the best ones that are available for use.

Acknowledgments. We are thankful to Prof. David Mitchell of the Desert Research Institute for providing the photographs of ice crystals and drops. This work was sponsored under U.S. Department of Energy Contracts DE-SC0004024 (ISDAC) and DE-SC0007035 (SPARTICUS) and National Aeronautics and Space Administration Contract NNX14AQ55G (SEAC^{4}RS).

REFERENCES

Baker, B. A., and R. P. Lawson, 2006: Improvement in determination of ice water content from two-dimensional particle imagery. Part I: Image-to-mass relationships. *J. Appl. Meteor.*, **45**, 1282–1290, doi:10.1175/JAM2398.1.

Mitchell, D. L., R. Zhang, and R. L. Pitter, 1990: Mass-dimensional relationships for ice particles and the influence of riming on snowfall rates. *J. Appl. Meteor.*, **29**, 153–163, doi:10.1175/1520-0450(1990)029<0153:MDRFIP>2.0.CO;2.